Article

O$_2$ Reduction at a DMSO/Cu(111) Model Battery Interface

Angelika Demling, Sarah B. King,* Philip Shushkov, and Julia Stähler*

Cite This: *J. Phys. Chem. C* 2023, 127, 2894−2900

Read Online

ACCESS | 📊 Metrics & More | 📖 Article Recommendations | 🆘 Supporting Information

ABSTRACT: To develop a better understanding of electro-chemical O$_2$ reduction in nonaqueous solvents, we apply two-photon photoelectron spectroscopy to probe the dynamics of O$_2$ reduction at a DMSO/Cu(111) model battery interface. By analyzing the temporal evolution of the photoemission signal, we observe the formation of O$_2^-$ from a trapped electron state at the DMSO/vacuum interface. We find the vertical binding energy of O$_2^-$ to be 3.80 ± 0.05 eV, in good agreement with previous results from electrochemical measurements, but with improved accuracy, potentially serving as a basis for future calculations on the kinetics of electron transfer at electrode interfaces. Modeling the O$_2$ diffusion through the DMSO layer enables us to quantify the activation energy of diffusion (31 ± 6 meV), the diffusion constant

(1 ± 1 × 10^{-8} cm^2/s), and the reaction quenching distance for electron transfer to O$_2$ in DMSO (12.4 ± 0.4 Å), a critical value for evaluating possible mechanisms for electrochemical side reactions. These results ultimately will inform the development and optimization of metal−air batteries in nonaqueous solvents.
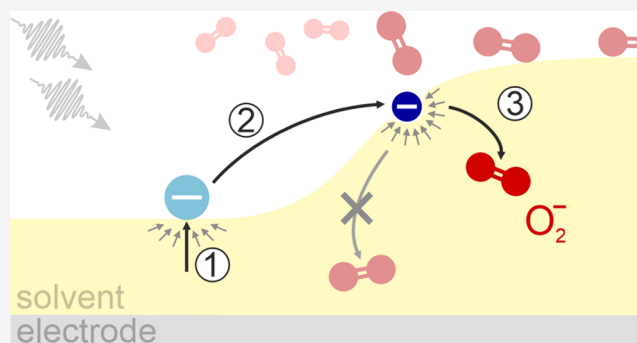
INTRODUCTION

O$_2$ reduction reactions (ORRs) are one half of the principle reactions of metal−air batteries, which promise extraordinarily high energy storage density from earth-abundant materials. However, numerous issues hinder large scale industrial use, from competing side reactions at the oxygen reduction electrode that form insulating, insoluble, O$_2$-containing salts to high overpotentials for oxygen reduction due to sluggish oxygen reduction kinetics.[1] Developing the precise solvent and electrolyte systems to promote desired reactivity and hinder side reactions is crucial for developing metal−air battery technology but often relies upon trial and error methods as we have a limited understanding of the fundamental distances and reaction energies relevant for oxygen reactivity at electrode interfaces.

Dimethyl sulfoxide (DMSO) is a nonaqueous solvent that has attracted attention as a solvent in lithium−,[2−5] zinc−,[6] and sodium−air batteries,[7] because of its role in modifying the energies of critical intermediates of the ORR. It is proposed that DMSO stabilizes O$_2^-$ at a distance far enough from the electrode to prevent the formation of O$_2^{2-}$ and the insulating, insoluble, O$_2$-containing electrode passivation side prod-ucts.[5,8,9] Molecular dynamics (MD) simulations predict that, immediately after the ORR, O$_2^-$ is pushed approximately 10 Å away from the electrode at negative cathode potentials, making a second electron transfer unlikely.[10] Determining the thickness of DMSO that prevents electron transfer to O$_2$, and therefore how far O$_2^-$ needs to be away from an electrode to *not* react, is critical to designing DMSO-based electrolytes

for metal−air batteries but is currently unknown and a focus of this work.

The Marcus theory of electron transfer has been used to predict the kinetics of electron transfer at electrode interfaces.[11−13] However, successful application of the theory requires accurate information about the energies of donor and acceptor species both before and after electron transfer, such as vertical binding energies and adiabatic electron affinities, to calculate the reorganization energy and energy of reaction that determines the interfacial reaction rate. The relevant energies for O$_2$ and O$_2^-$ in DMSO have been estimated from the O$_2$/O$_2^-$ redox potential in DMSO measured with cyclic voltammetry (CV). The O$_2$/O$_2^-$ redox potential ranges from −0.73 V in a 0.1 M (Et)$_4$NClO$_4$−DMSO solution with respect to a standard calomel electrode (SCE)[14] to 2.7 V in a 0.1 M TBAClO$_4$−DMSO solution versus Li/Li$^+$ using *in situ* surface-enhanced Raman spectroscopy (SERS) measurements.[15] These redox potentials can be compared to the vacuum level of the working electrode through the standard hydrogen electrode and its vacuum level (details in the Supporting Information)[16−18] but result in a fairly wide range of energies as shown in Figure 1(a) (first two columns). These factors make the accurate
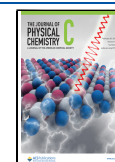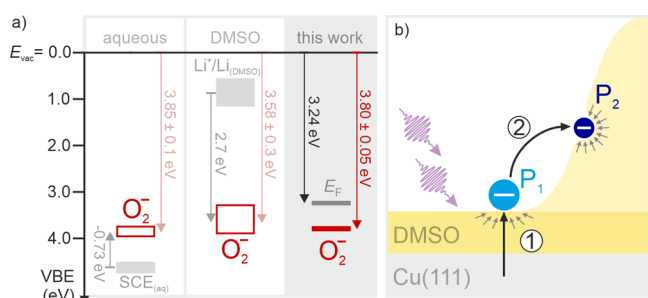
Figure 1. (a) Energy level alignment of O_2^- relative to E_{vac} based on electrochemical[14−16,18] (red-bounded) and photoemission experiments (red). (b) Illustration of photoinduced polaron formation (process 1) at the surface of the two wetting monolayers of DMSO and subsequent electron trapping at the multilayer/vacuum interface (process 2). P_1 and P_2 denote the respective spectral signatures.

determination of the vertical binding energy (VBE) of O_2^- in DMSO challenging and prevent accurate modeling of electron transfer reactions at electrode surfaces.

Owing to their importance in a variety of research fields, electron solvation processes have been the subject of numerous studies in the ultrafast time domain applying optical and terahertz spectroscopy as well as photoemission.[19−24] Two-photon photoemission (2PPE) spectroscopy of solvent molecular layers has been used to probe the energies, solvation dynamics, and reactivity of electronic states in molecular layers ranging from H_2O, NH_3, and organic solvents such as DMSO to liquid crystals.[25−33] By using ultrafast laser pulses to create excited electrons above the Fermi level of a metal substrate, nonequilibrium electrons can be injected into adsorbed molecular layers and probed using a second laser pulse delayed by femtoseconds to microseconds. Using this strategy, 2PPE has been able to observe the 10s to 100s of femtoseconds formation of small polarons in DMSO. In a previous publication, we discuss the electron transfer from these electronic states located on two wetting monolayers of DMSO to much longer-living electronic states located on thicker DMSO islands with lifetimes on the order of seconds.[31] A cartoon of the transfer process is displayed in Figure 1(b). Furthermore, 2PPE is capable of determining the population dynamics of such long-lived states by applying pump−wait−probe experiments (cf. Supporting Information) or measuring the repetition rate dependence of the respective feature.[34−36] Even chemical reactions involving long-lived "trapped" electrons can be detected in 2PPE experiments. For example, on water−ice surfaces, it was shown that trapped electrons can react with coadsorbed molecules, breaking H−OH and Cl−CCl$_2$F bonds and generating highly reactive hydroxide and chloride ions.[25,26,37]

In this paper, we use monochromatic 2PPE of O_2 adsorbed on DMSO molecular layers on Cu(111) to probe the electronic states of DMSO and O_2 at a model electrode interface. We show that trapped electrons of DMSO (P_2 shown in Figure 1(b)) serve as a precursor for O_2^- formation. We measure the VBE of O_2^- to be 3.80 ± 0.05 eV.

By investigating the electron transfer dynamics from the trapped electron state in DMSO to O_2, i.e., the first ORR, along with modeling O_2 diffusion into the DMSO adlayer, we can observe the distance dependence of O_2 reduction and identify the reaction quenching distance for electron transfer in DMSO. Through these experiments we have determined two components critical for accurate models of electrochemical

systems with DMSO and O_2, the VBE of O_2^-, and its formation distance, which will direct research efforts to prevent electrode passivation by unwanted oxygen reduction pathways.

■ METHODS

The Cu(111) crystal is prepared by repeated cycles of sputtering at 0.75 kV with 1.5×10^{-6} mbar Ar$^+$ ions for 10 min followed by annealing at 800 K for 45 min. The surface cleanliness and order is verified by LEED, work function (Φ) measurements, and the width and intensity of the surface state characteristic for Cu(111) in 2PPE spectra.[38] The ≥99.9% anhydrous DMSO (Sigma-Aldrich) is attached to the gas manifold of the ultrahigh vacuum system in an argon atmosphere and cleaned by numerous freeze−pump−thaw cycles. Its cleanliness is confirmed by residual gas analysis. The DMSO molecules are deposited onto the copper substrate through a pinhole doser with a diameter of 5 μm and a backing pressure of 6×10^{-1} mbar. First, molecules are deposited for 210 s with the Cu crystal temperature held at 200 K. Afterward the sample is annealed for 10 min at 210 K before further molecules are deposited at 150 K for 135 s, followed by a second annealing at 180 K for 10 min. As discussed previously,[31] using this method, a reproducible adsorption of two crystalline DMSO monolayers partially covered with multilayer islands is achieved and the nominal layer thickness is verified with thermal desorption spectroscopy. More information about sample preparation and characterization of DMSO adlayers can be found in a previous publication and its corresponding supporting information.[31] O_2 molecules are adsorbed onto the DMSO/Cu(111) sample by background dosing at 46 K. At this temperature, only a monolayer of O_2 can be physisorbed on the surface.[39] All referenced temperatures are measured using a K-type thermocouple inside the copper crystal.

The laser system is a Light Conversion Pharos pump laser combined with a nonlinear optical parametric amplifier (Orpheus 2H) operating at 200 kHz. This system delivers ultrashort laser pulses tunable from the visible to near UV. In the described experiments, photon energies between 2.9 and 3.2 eV are used, with pulse durations of approximately 100 fs.

Monochromatic 2PPE is a surface-sensitive technique that can determine the energies of both occupied and normally unoccupied electronic states with respect to the Fermi and vacuum level of the sample. The working principle is depicted in Figure 2(a). In 2PPE, the absorption of two photons ionizes the sample and generates photoelectrons with finite kinetic energies with respect to the vacuum level, E_{vac}. The kinetic energies, E_{kin}, of the photoemitted electrons are measured with a hemispherical electron analyzer (SPECS Phoibos 100). The energy resolution of the experimental setup is better than 50 meV and determined by the spectral width of the laser pulse and the resolution of the analyzer. If the 2PPE process occurs via a real, normally unoccupied, so-called *intermediate* state above the Fermi energy, E_F, variation of the photon energy by $\Delta h\nu$ will shift the peak by this value in the 2PPE spectra (left in Figure 2(a)). If there is no real intermediate state, and the photoemission intensity results from an occupied *initial* state below E_F, variation of the photon energy by $\Delta h\nu$ will shift the 2PPE peak by $2\Delta h\nu$ (right in Figure 2(a)).

The energy of 2PPE features can be expressed in relation to different reference levels based on the measurement of the kinetic energy of the photoelectrons, the independent determination of E_F and Φ of the sample: The final state
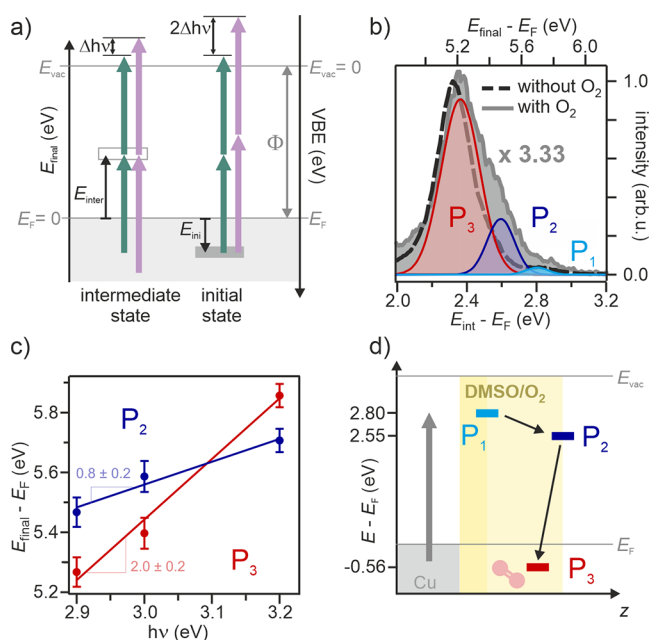
Figure 2. (a) Monochromatic 2PPE schematic. The green and purple arrows show different photon energies for distinguishing intermediate and initial states in 2PPE spectra. (b) Steady-state 2PPE spectrum of 4 ML of DMSO on Cu(111) with (solid) and without (dashed) O_2 adsorption. The shaded red (P_3), dark blue (P_2), and light blue (P_1) curves are Gaussians fitted to the 2PPE spectrum of the O_2 dosed sample. (c) Final state energy of P_2 and P_3 versus photon energy averaged over four different fluences. The error bars refer to the standard deviations of the fits for individual measurements. (d) Energy level alignment for multilayer DMSO on Cu(111) with additional O_2 adsorption. After the small polaron (P_1, light blue) is formed, the electron can become trapped (P_2, dark blue) and react with O_2 to form O_2^- (P_3, red).

energy, E_{final} (Figure 2(a), left axis), provides the excess energy of the photoelectrons with respect to E_F

$$E_{final} = E_{kin} + \Phi \qquad (1)$$

where E_F is determined at a gold surface in electrical contact with the sample. Φ is given by the half-maximum of the intensity of the 2PPE spectrum's low-energy cutoff on the final state energy axis as discussed in detail previously.[40] The intermediate and initial state energies, E_{int} and E_{ini}, respectively, are

$$E_{int} = E_{final} - h\nu \qquad (2)$$

$$E_{ini} = E_{final} - 2h\nu < 0 \qquad (3)$$

Finally, the VBE (Figure 2(a), right axis) with respect to E_{vac} is useful when comparing energy levels to electrochemical data and is calculated by

$$VBE = \Phi - E \qquad (4)$$

where E either denotes the intermediate or initial state energy, depending on the character of the investigated state, both with respect to $E_F = 0$.

■ RESULTS

Energy Level Alignment of O_2-Related States. Adsorption of O_2 on top of 4 ML of DMSO on Cu(111) modifies the electronic states measured by 2PPE spectroscopy and their energy level alignment. Figure 2(b) shows the

monochromatic 2PPE spectra of DMSO/Cu(111) with and without O_2 relative to the final (top) and intermediate state energy axis (bottom). The spectrum with O_2 (gray) is notably broader to the high-energy side than the one without O_2 (dashed) and can be fit with three Gaussian peaks shown in light blue, dark blue, and red and referred to as P_1, P_2, and P_3, respectively. A comparison between the data and the corresponding fit is shown in the Supporting Information. P_1 at E_{int} = 2.8 eV with respect to E_F is consistent with the transient small polaron in DMSO with the same energy level alignment as in the absence of O_2.[31]

To assign P_2 and P_3 to initial or intermediate electronic states, we measured 2PPE spectra of O_2/DMSO/Cu(111) as a function of photon energy for four different fluences each. The peak positions of P_2 and P_3 as a function of photon energy are shown in Figure 2(c). As the photon energy is changed, P_3 shifts with approximately $2\Delta h\nu$ while P_2 shifts with approximately $\Delta h\nu$, meaning that P_3 is an initial and P_2 is an intermediate state. Based on this, we determine the intermediate state energy of P_2 to be $E_{int}(P_2)$ = 2.55 ± 0.03 eV and the initial state energy of P_3 to be $E_{ini}(P_3) = -0.56$ ± 0.03 eV with respect to E_F.

$E_{int}(P_2)$ is very similar to the intermediate state energy of the trapped electron of 2.34 eV observed previously[31] on DMSO/ Cu(111) *without* O_2. As in this previous work, the lifetime of P_2 is also on the order of several seconds, as expected (cf. Introduction) and shown in the Supporting Information. We, therefore, assign P_2 to a long-lived surface trapped electron (e_T) of the O_2/DMSO surface. E_{int} of e_T for the O_2/DMSO surface is approximately 200 meV higher in energy than for the pure DMSO surface. This suggests a destabilization of the trapped electron due to the presence of oxygen.

The VBE of P_3 is 3.80 ± 0.05 eV, determined using eq 4 and the measured O_2/DMSO/Cu(111) work function of Φ = 3.24 ± 0.05 eV. We directly compare this binding energy to the approximate values of the energy of the O_2/O_2^- half reaction in DMSO obtained from cyclic voltammetry.[14,15] Using literature values for the normal hydrogen electrode (NHE) with respect to E_{vac} combined with the relative energies of the saturated calomel electrode (SCE) and the Li/Li^+ half reaction with respect to NHE and a correction for the use of different solvents, the CV data can be compared to E_{vac}, as shown in Figure 1(a) and Figure S1.[17,18] A detailed description of how the electrode potentials are related to the vacuum potential is given in the Supporting Information. CV experiments estimate the VBE of O_2^- between 3.28 and 3.95 eV, i.e., overlapping with the VBE of P_3 measured in this work.[14,15,41] Moreover, theoretical calculations of O_2^- solvated in DMSO (Supporting Information) determine a VBE between 3.55 and 3.66 eV, in good agreement with our measured P_3. Based on the appearance of P_3 only on O_2-exposed surfaces and similarity with CV measurements and theoretical calculations, we assign P_3 to photoemission from O_2^-, superoxide. The differences between our measured VBE and those estimated from CV are well within the possible errors due to reference electrode to vacuum level calibration and the influence of electrolyte.[14,15,41]

Mechanism of O_2 Reduction. Solvent layers effectively screen adsorbed molecular species and electronic states from the metal substrate and often inhibit direct electron transfer through wave function overlap; for reactant molecules adsorbed on insulating solvent surfaces (such as DMSO), a precursor electronic state in the solvent, ideally with a long lifetime, is usually needed for electron transfer leading to anion

formation from the reactant molecule.[25,26,31] To determine whether the short-lived small polaron or the long-lived e_T is a precursor state to O_2^-,[31] we took 2PPE spectra for O_2-exposed surfaces as a function of DMSO coverage. At low DMSO coverages, where e_T is not present, but there is a prominent signature of the small polaron,[31] the spectroscopic signature of O_2^-, P_3, is not observed (not shown). Only at sufficiently high DMSO coverages above 2 ML where e_T is observed does the O_2^- signature appear. Therefore, we conclude that e_T is the precursor state of O_2^-, as sketched in Figure 2(d), in analogy to previous work on reactivity of surface-trapped electrons at water-ice surfaces.[26,37]

To determine the mechanism of O_2^- formation, we investigated the time-dependence of O_2^- formation by measuring 2PPE spectra as a function of surface illumination time. Real-time measurements, instead of ultrafast stroboscopic measurements, are required due to the lifetime of e_T that exceeds the inverse repetition rate of our laser system, 5 μs. Figure 3(a) shows a representative series of 2PPE spectra of
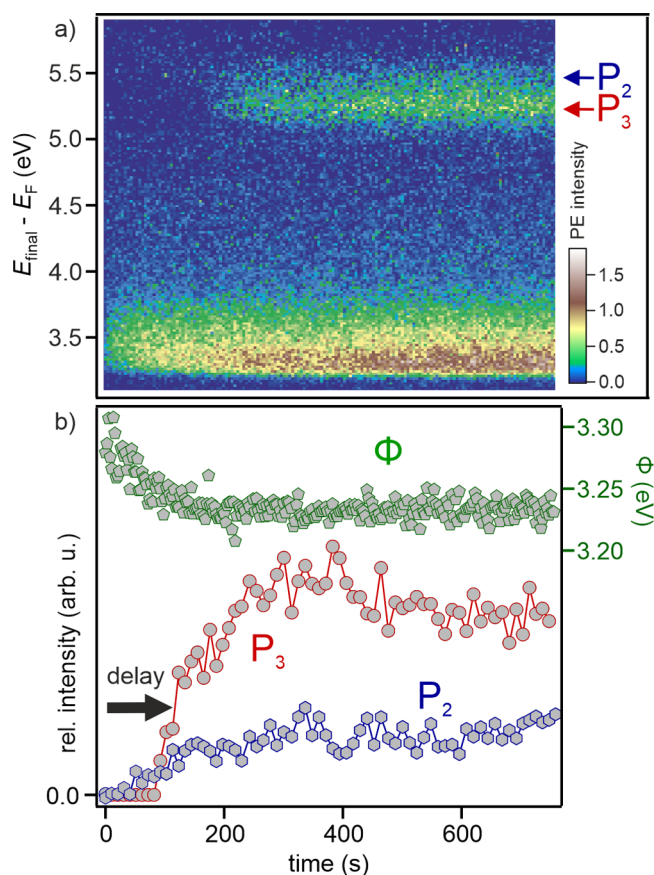

Figure 3. (a) 2PPE spectra of an $O_2/DMSO/Cu(111)$ sample as a function of real-time illumination in false colors. The blue and red arrows indicate the positions of P_2 and P_3 signatures, respectively. (b) Evolution of Φ, P_2 and P_3 intensity as a function of illumination time from the data in panel a.

$O_2/DMSO/Cu(111)$ as a function of illumination time in false colors measured with $h\nu = 2.9$ eV with a photon fluence of 2.1 μJ cm^{-2}. The spectral locations of e_T (P_2) and O_2^- (P_3) are shown by blue and red arrows, respectively. Both features appear after a delay of more than 100 s, in sharp contrast to the dynamics of e_T in the absence of O_2, where the trapped electron is formed on a subpicosecond time scale.[31] This

observation is highlighted in Figure 3(b), which displays intensities of e_T (P_2, blue) and O_2^- (P_3, red) extracted by Gaussian fits as in Figure 2(b) and Φ (green) as a function of illumination time. Qualitatively, the delayed rise of P_2 and P_3 is accompanied by a decrease in the sample work function.

To explore the origin of these unusual dynamics, we collected similar data sets for different photon energies and fluences, all of which can be found in the Supporting Information. We plot representative data for the fluence-dependent dynamics of e_T, O_2^-, and Φ for $h\nu = 2.9$ eV in Figure 4. As the fluence is increased, the populations of e_T and O_2^- increase, they appear at earlier illumination times, and the early time drop in the work function occurs faster.
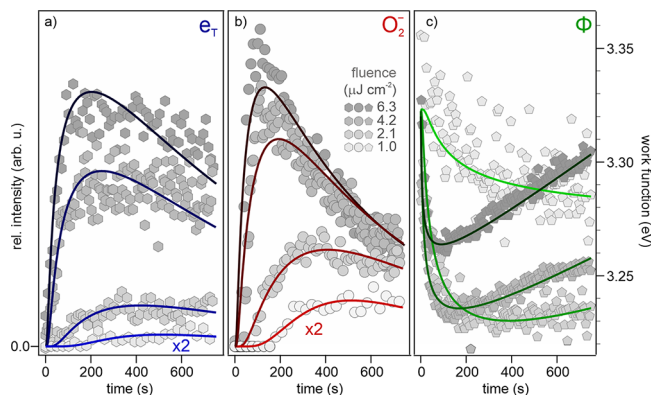

Figure 4. Evolution of (a) e_T and (b) O_2^- intensities, and (c) Φ measured with $h\nu = 2.9$ eV for four different fluences. The lines denote the fit results from a global fit described in the text.

Model of O_2 Diffusion in DMSO. We propose that the increase in amplitude of e_T and O_2^-, the decrease in their appearance time, and the faster Φ decrease observed with increasing photon fluence are all due to diffusion of O_2 into the DMSO layers and reactivity of e_T and O_2 to form O_2^-. We will now go through this proposed mechanism in detail.

e_T in DMSO are surface-bound electronic states, likely localized at defects within the topmost monolayer.[31] Adsorption of gases on the surface leads to a decrease and/or quenching of photoemission from these states due to dielectric squeezing or blocking of trapped electron binding sites.[25,31,42] At the same time, additional adsorbates may alter the surface potential and decrease or enhance the sample work function. The delayed appearance of e_T, accompanied by the work function decrease, suggests that something quenching e_T photoemission intensity and increasing the work function has been removed. As these observations only occur when O_2 is adsorbed, it seems evident that molecular oxygen is the source of both observations.

Both desorption of O_2 from the surface or diffusion into the DMSO layers—driven by heat supplied by the ultrafast laser system—could be the source of surface O_2 removal and lead to the delayed e_T intensity rise and work function decrease. However, if desorption were the cause, the spectrum after the delayed rise should coincide with a spectrum where O_2 was desorbed by heating the copper substrate above the desorption temperature of O_2 but below the one of DMSO. As shown in Figure S6 in the Supporting Information, this is not the case. Hence, we conclude that diffusion of O_2 into the DMSO layers is the cause for the appearance of e_T (c.f. illustration in Figure 5). In addition, decrease in the surface concentration of

O_2 through diffusion would also explain the drop in Φ that occurs on the same time scales as e_T and O_2^- appearance.
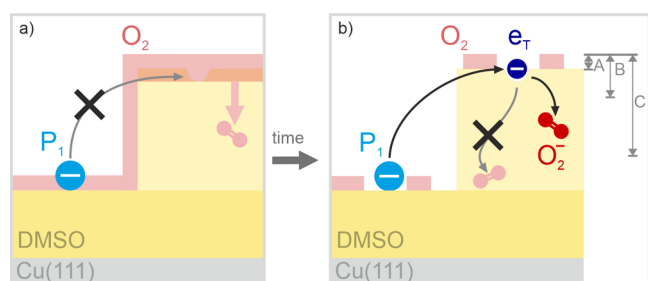

Figure 5. (a) Sketch of sample before illumination, T = 46 K. O_2 induces an interfacial dipole and blocks the trapping sites. Hence, no e_T formation is possible. (b) Sketch of sample under illumination, $T >$ 46 K. O_2 diffuses through the adsorbed DMSO. A, B, and C refer to different regions in DMSO as described in the text.

We are able to capture the O_2^- photoemission intensity changes with a simple model of O_2 diffusion in DMSO as follows. The diffusion of the O_2 layer into DMSO is approximated using Fick's law of diffusion in one dimension where all diffusion occurs from the surface into DMSO. In most solids, the diffusion constant $D(T)$ follows an Arrhenius law

$$D(T) = D_0 \times \exp\left(-\frac{E_{\text{diff}}}{k_B T}\right) \tag{5}$$

where the diffusion depends on an effective temperature, which in our experiments is determined by the photon fluence and is higher than the equilibrium temperature of the sample. We simplify the system into three regions shown graphically in Figure 5(b): the monolayer of adsorbed oxygen A that contributes to the formation of an interfacial dipolar layer and modifies the work function, the region B where near-surface oxygen can still block electron trapping sites, and the reaction region C where the distance of O_2 from the surface is small enough that there is sufficient wave function overlap for electron transfer from e_T to O_2. Once the O_2 molecules have diffused beyond C, they cannot be reduced anymore, and the reaction is quenched.

The photoemission signals from e_T and O_2^-, P_2, and P_3, respectively, can both be fit using differential equations that account for the photoexcitation and photoemission processes, diffusion of oxygen and reaction of the trapped electron with O_2 forming O_2^-. Both are proportional to the incident laser fluence, F, and the time-dependent number of accessible sites for e_T formation, $N_{\text{acc}}(t)$

$$I_{e_T} \propto F \times N_{\text{acc}}(t) \tag{6}$$

$$I_{O_2^-} \propto F \times N_{\text{acc}}(t) \times n_C(t) \tag{7}$$

where the proportionality constants are determined by the different cross sections for photoexcitation and photoemission, and $n_C(t)$ describes the number of O_2 molecules within the region C. The density of accessible sites for e_T formation

$$N_{\text{acc}}(t) = N_S(t) \times \left(1 - \frac{n_B(t)}{n_{O_2}}\right) \tag{8}$$

depends on the density of electron trapping sites $N_S(t)$, which decreases exponentially with time due to healing of surface defects as observed previously for e_T on crystalline D_2O on Ru(001).[43] The ratio $n_B(t)/n_{O_2}$ describes the fraction of oxygen molecules in the region B that contribute to blocking of trapping sites, i.e., $N_{\text{acc}}(t)$ is the fraction of unblocked trapping sites for e_T.

The time-dependence of Φ is fit by considering the number of oxygen molecules $n_A(t)$ that remain in the surface region A

$$\Delta\Phi(t) = \mu n_A(t) \tag{9}$$

where each surface oxygen molecule contributes a small interfacial dipole μ that modifies the work function. All of the equations used in the fitting and their detailed explanations can be found in the Supporting Information.

Using this simple diffusion model, we can globally fit the dynamics of e_T and O_2^- across all of the fluences and photon energies. Φ is also included in the global fit at 2.9 eV, but not at 3.0 and 3.2 eV, as the early time work function changes at those photon energies occur too quickly to be captured in our experiments, as detailed in the Supporting Information. As shown in Figure 4 and Figure S8, the global fit shows an excellent agreement with the data. From this, we extract the activation energy of diffusion, E_{diff} = 31 ± 6 meV and the temperature-independent diffusion constant of O_2 in solid DMSO, $D_0 = (1 \pm 1) \times 10^{-20}$ cm^2/pulse, which can be translated to $D_0 = (1 \pm 1) \times 10^{-8}$ cm^2/s assuming that each laser pulse heats the surface for approximately 1 ps until the heat is dissipated in the metal substrate through electron–electron and electron–phonon scattering.[44] To our knowledge, this is the first time that D_0 and E_{diff} of O_2 diffusion in solid DMSO have been measured. For O_2 diffusion in amorphous solid water, similar values were found.[45]

In the diffusion model, the regions A, B, and C are dependent upon one another, and one region must be set. A is the region where the oxygen interfacial dipole modifies the sample work function, which we set to the van der Waals radius of an oxygen atom, 1.54 Å,[46] as a reasonable minimum distance of the width of the one monolayer of oxygen molecules that forms on the DMSO surface at our deposition temperature of 46 K. Based on this, our global fit yields B = 4.4 ± 0.1 Å and C = 14.0 ± 0.4 Å. From these distances, we can calculate the DMSO thickness needed to prevent O_2 blocking of e_T trapping sites, B − A, is 2.8 ± 0.6 Å, and the thickness of DMSO needed to prevent electron transfer to O_2, $x_{\text{react}} = $ C − A, is 12.4 ± 0.4 Å. Since the distances B, C, and x_{react} are proportional to A, the extracted values from the modeling must also be considered as minimum distances.

We can compare these values with other known distances for DMSO solvation. The radial pair distribution function obtained from X-ray diffraction and molecular dynamics calculations of solid and liquid DMSO describes how DMSO organizes around other DMSO molecules or around solutes, such as O_2 and e_T studied here. The first coordination shell of liquid DMSO is found between 3 and 5 Å from other DMSO molecules and solutes.[10,47] Consistent with this, our experiments found that when O_2 was within B − A = 2.8 ± 0.6 Å, from the surface, i.e., within the first solvation shell of surface-trapped electrons e_T, it could suppress the e_T signal. Furthermore, the end of the third coordination shell of DMSO is approximately 11−12 Å.[10,47] This value is in good agreement with the reaction quenching distance, x_{react}, that we

determined to be the thickness of DMSO that inhibits electron transfer to oxygen. In other words, on average three solvation shells of DMSO are required to sufficiently dampen the electron wave function (i.e., screen the excess electron) to prevent electron transfer from an electronic state such as the e_T in our experiments. It seems plausible that similar reaction quenching distances would apply for electron transfer from an electrode surface to O_2 or O_2^-.

The reaction quenching distance for electron transfer in DMSO helps determine the possible mechanisms for the formation of unwanted side products in metal–air batteries. Simulations by Sergeev et al.[10] found that O_2^- sits between 10 and 12 Å away from the cathode, far enough away that our experiments suggest DMSO could significantly suppress electron transfer. In contrast, LiO_2, which has a high concentration 7 Å from the cathode surface,[10] is unlikely to be protected from further reduction by DMSO alone because, from our experiments, 7 Å of DMSO are insufficient to prevent electron transfer by screening. Our experiments therefore corroborate the conclusion of Sergeev et al.[10] that reduction of LiO_2 to LiO_2^- is a more likely source of electrode passivation in Li–Air batteries than O_2^{2-} formation and suggests that the screening of DMSO plays a significant role in this mechanism.

CONCLUSION

In conclusion, we report the formation of O_2^- near a DMSO/Cu(111) model battery interface. We were able to directly measure that the VBE of O_2^- solvated by DMSO is 3.80 ± 0.05 eV with great accuracy, which may serve as a basis for future calculations on the kinetics of electron transfer at electrode interfaces. We also determined the energy barrier of oxygen diffusion and the diffusion constant in solid DMSO, the reaction quenching distance, x_{react}, of electron transfer in DMSO, which suppresses O_2 reduction after approximately 12 Å (approximately three solvation shells of DMSO). Optimizing the electrolyte system to allow for optimal O_2^- formation but suppressing side reactions such as O_2^{2-} and LiO_2^- formation could prevent Li–air battery electrode passivation, a limitation to their repeated use. Our experiments can inform the selection of solvents for battery electrolytes in general by demonstrating the degree of screening required to prevent reduction between diffuse electronic states and small molecular species in solution, an important design criterion.

ASSOCIATED CONTENT

ⓈI Supporting Information

The Supporting Information is available free of charge at https://pubs.acs.org/doi/10.1021/acs.jpcc.2c07491.

> Conversion between electrochemical potentials and the vacuum level. Shuttering experiments and decrease in trapped electron lifetime by O_2. Fit of steady-state 2PPE spectrum from O_2/DMSO/Cu(111). Diffusion vs desorption of O_2. Derivation of diffusion model (PDF)

AUTHOR INFORMATION

Corresponding Authors

    Sarah B. King — *Department of Physical Chemistry, Fritz Haber Institute of the Max Planck Society, 14195 Berlin, Germany;* Present Address: Department of Chemistry and James Franck Institute, University of Chicago, Chicago. Illinois 60637; orcid.org/0000-0003-0274-9894; Email: sbking@uchicago.edu

    Julia Stähler — *Department of Physical Chemistry, Fritz Haber Institute of the Max Planck Society, 14195 Berlin, Germany; Humboldt-Universität zu Berlin, Institut für Chemie, 12489 Berlin, Germany;* orcid.org/0000-0002-3005-4697; Email: staehler@fhi-berlin.mpg.de

Authors

    Angelika Demling — *Department of Physical Chemistry, Fritz Haber Institute of the Max Planck Society, 14195 Berlin, Germany; Humboldt-Universität zu Berlin, Institut für Chemie, 12489 Berlin, Germany*

    Philip Shushkov — *Department of Chemistry, Tufts University, Somerville, Massachusetts 02155, United States;* Present Address: Department of Chemistry, Indiana University, Bloomington, Indiana 47405.

Complete contact information is available at:
https://pubs.acs.org/10.1021/acs.jpcc.2c07491

ACKNOWLEDGMENTS

REFERENCES

(1) Salado, M.; Lizundia, E. Advances, challenges and environmental impacts in metal–air battery electrolytes. *Materials Today Energy* **2022**, *28*, 101064.

(2) Khan, A.; Zhao, C. Enhanced performance in mixture DMSO/ionic liquid electrolytes: Toward rechargeable Li–O₂ batteries. *Electrochem. Commun.* **2014**, *49*, 1–4.

(3) Liu, T.; Vivek, J. P.; Zhao, E. W.; Lei, J.; Garcia-Araez, N.; Grey, C. P. Current Challenges and Routes Forward for Nonaqueous Lithium–Air Batteries. *Chem. Rev.* **2020**, *120*, 6558–6625.

(4) Peng, Z.; Freunberger, S. A.; Chen, Y.; Bruce, P. G. A Reversible and Higher-Rate Li-O₂ Battery. *Science* **2012**, *337*, 563–566.

(5) Johnson, L.; Li, C.; Liu, Z.; Chen, Y.; Freunberger, S. A.; Ashok, P. C.; Praveen, B. B.; Dholakia, K.; Tarascon, J.-M.; Bruce, P. G. The role of LiO₂ solubility in O₂ reduction in aprotic solvents and its consequences for Li–O₂ batteries. *Nat. Chem.* **2014**, *6*, 1091–1099.

(6) Hosseini, S.; Abbasi, A.; Uginet, L.-O.; Haustraete, N.; Praserthdam, S.; Yonezawa, T.; Kheawhom, S. The Influence of Dimethyl Sulfoxide as Electrolyte Additive on Anodic Dissolution of Alkaline Zinc-Air Flow Battery. *Sci. Rep.* **2019**, *9*, 14958 DOI: 10.1038/s41598-019-51412-5.

(7) Dilimon, V. S.; Hwang, C.; Cho, Y.-G.; Yang, J.; Lim, H.-D.; Kang, K.; Kang, S. J.; Song, H.-K. Superoxide stability for reversible Na-O₂ electrochemistry. *Sci. Rep.* **2017**, *7*, 17635.

(8) Laoire, C. O.; Mukerjee, S.; Abraham, K.; Plichta, E. J.; Hendrickson, M. A. Influence of nonaqueous solvents on the electrochemistry of oxygen in the rechargeable lithium-air battery. *J. Phys. Chem. C* **2010**, *114*, 9178–9186.

(9) Kwabi, D. G.; Bryantsev, V. S.; Batcho, T. P.; Itkis, D. M.; Thompson, C. V.; Shao-Horn, Y. Experimental and Computational Analysis of the Solvent-Dependent O₂/Li⁺-O₂⁻ Redox Couple: Standard Potentials, Coupling Strength, and Implications for Lithium–Oxygen Batteries. *Angew. Chem., Int. Ed.* **2016**, *55*, 3129–3134.

(10) Sergeev, A. V.; Chertovich, A. V.; Itkis, D. M.; Sen, A.; Gross, A.; Khokhlov, A. R. Electrode/Electrolyte Interface in the Li–O₂ Battery: Insight from Molecular Dynamics Study. *J. Phys. Chem. C* **2017**, *121*, 14463–14469.

(11) Marcus, R. A. On the theory of electron-transfer reactions. VI. Unified treatment for homogeneous and electrode reactions. *J. Chem. Phys.* **1965**, *43*, 679−701.

(12) Henstridge, M. C.; Laborda, E.; Rees, N. V.; Compton, R. G. Marcus−Hush−Chidsey theory of electron transfer applied to voltammetry: A review. *Electrochim. Acta* **2012**, *84*, 12−20.

(13) Albery, W. J. The application of the Marcus relation to reactions in solution. *Annu. Rev. Phys. Chem.* **1980**, *31*, 227−263.

(14) Sawyer, D. T.; Roberts, J. L. Electrochemistry of oxygen and superoxide ion in dimethylsulfoxide at platinum, gold and mercury electrodes. *J. Electroanal. Chem.* **1959**, *1966* (12), 90−101.

(15) Peng, Z.; Chen, Y.; Bruce, P. G.; Xu, Y. Direct Detection of the Superoxide Anion as a Stable Intermediate in the Electroreduction of Oxygen in a Non-Aqueous Electrolyte Containing Phenol as a Proton Source. *Angew. Chem., Int. Ed.* **2015**, *54*, 8165−8168.

(16) Trasatti, S. The absolute electrode potential: an explanatory note (Recommendations 1986). *Pure Appl. Chem.* **1986**, *58*, 955−966.

(17) Bard, A. J.; Faulkner, L. R.; White, H. S.*Electrochemical methods: fundamentals and applications*; John Wiley & Sons: New York, NY, 2001.

(18) Fawcett, W. R. The ionic work function and its role in estimating absolute electrode potentials. *Langmuir* **2008**, *24*, 9868−9875.

(19) Alfano, J. C.; Walhout, P.; Kimura, Y.; Barbara, P. F. Ultrafast transient-absorption spectroscopy of the aqueous solvated electron. *J. Chem. Phys.* **1993**, *98*, 5996−5998.

(20) Kimura, Y.; Alfano, J. C.; Walhout, P.; Barbara, P. F. Ultrafast transient absorption spectroscopy of the solvated electron in water. *J. Phys. Chem.* **1994**, *98*, 3450−3458.

(21) Shi, X.; Long, F. H.; Lu, H.; Eisenthal, K. B. Femtosecond electron solvation kinetics in water. *J. Phys. Chem.* **1996**, *100*, 11903−11906.

(22) Knoesel, E.; Bonn, M.; Shan, J.; Wang, F.; Heinz, T. F. Conductivity of solvated electrons in hexane investigated with terahertz time-domain spectroscopy. *J. Chem. Phys.* **2004**, *121*, 394−404.

(23) Bruggeman, P. J.; Frontiera, R. R.; Kortshagen, U. R.; Kushner, M. J.; Linic, S.; Schatz, G. C.; Andaraarachchi, H.; Exarhos, S.; Jones, L. O.; Mueller, C. M.; et al. Plasma-driven solution electrolysis. *J. Appl. Phys.* **2021**, *129*, 200902.

(24) Ban, L.; Yoder, B. L.; Signorell, R. Size-Resolved Electron Solvation in Neutral Water Clusters. *J. Phys. Chem. A* **2021**, *125*, 5326−5334.

(25) Bertin, M.; Meyer, M.; Stähler, J.; Gahl, C.; Wolf, M.; Bovensiepen, U. Reactivity of water−electron complexes on crystalline ice surfaces. *Faraday Discuss.* **2009**, *141*, 293−307.

(26) King, S. B.; Wegkamp, D.; Richter, C.; Wolf, M.; Stähler, J. Trapped Electrons at the Amorphous Solid Water/Vacuum Interface as Possible Reactants in a Water Splitting Reaction. *J. Phys. Chem. C* **2017**, *121*, 7379−7386.

(27) Stähler, J.; Meyer, M.; Kusmierek, D. O.; Bovensiepen, U.; Wolf, M. Ultrafast electron transfer dynamics at NH_3/Cu(111) interfaces: Determination of the transient tunneling barrier. *J. Am. Chem. Soc.* **2008**, *130*, 8797−8803.

(28) Kwon, H.; Hwang, K.; Park, J.; Ryu, S.; Kim, S. K. Electron solvation and solvation-induced crystallization of an ammonia film on Ag(111) studied by 2-photon photoemission. *Phys. Chem. Chem. Phys.* **2011**, *13*, 17785−17790.

(29) Li, B.; Zhao, J.; Onda, K.; Jordan, K. D.; Yang, J.; Petek, H. Ultrafast interfacial proton-coupled electron transfer. *Science* **2006**, *311*, 1436−1440.

(30) Strader, M. L.; Garrett-Roe, S.; Szymanski, P.; Shipman, S. T.; Johns, J. E.; Yang, A.; Muller, E.; Harris, C. B. The ultrafast dynamics of image potential state electrons at the dimethylsulfoxide/Ag(111) interface. *J. Phys. Chem. C* **2008**, *112*, 6880−6886.

(31) King, S. B.; Broch, K.; Demling, A.; Stähler, J. Multistep and multiscale electron transfer and localization dynamics at a model electrolyte/metal interface. *J. Chem. Phys.* **2019**, *150*, 041702.

(32) Miller, A. D.; Bezel, I.; Gaffney, K. J.; Garrett-Roe, S.; Liu, S. H.; Szymanski, P.; Harris, C. B. Electron solvation in two dimensions. *Science* **2002**, *297*, 1163−1166.

(33) Muller, E. A.; Strader, M. L.; Johns, J. E.; Yang, A.; Caplins, B. W.; Shearer, A. J.; Suich, D. E.; Harris, C. B. Femtosecond electron solvation at the ionic liquid/metal electrode interface. *J. Am. Chem. Soc.* **2013**, *135*, 10646−10653.

(34) Bovensiepen, U.; Gahl, C.; Stähler, J.; Bockstedte, M.; Meyer, M.; Baletto, F.; Scandolo, S.; Zhu, X.-Y.; Rubio, A.; Wolf, M. A Dynamic Landscape from Femtoseconds to Minutes for Excess Electrons at Ice- Metal Interfaces. *J. Phys. Chem. C* **2009**, *113*, 979−988.

(35) Gierster, L.; Vempati, S.; Stähler, J. Ultrashort and metastable doping of the ZnO surface by photoexcited defects. *Faraday Discuss.* **2022**, *237*, 58.

(36) Vempati, S.; Bogner, L.; Richter, C.; Deinert, J.-C.; Foglia, L.; Gierster, L.; Stähler, J. Photoexcited organic molecules en route to highly efficient autoionization. *J. Chem. Phys.* **2020**, *152*, 074715.

(37) Stähler, J.; Gahl, C.; Wolf, M. Dynamics and Reactivity of Trapped Electrons on Supported Ice Crystallites. *Acc. Chem. Res.* **2012**, *45*, 131−138.

(38) Reuß, C.; Shumay, I. L.; Thomann, U.; Kutschera, M.; Weinelt, M.; Fauster, T.; Höfer, U. Control of the Dephasing of Image-Potential States by CO Adsorption on Cu(100). *Phys. Rev. Lett.* **1999**, *82*, 153−156.

(39) Dohnálek, Z.; Kim, J.; Bondarchuk, O.; White, J. M.; Kay, B. D. Physisorption of N_2, O_2, and CO on Fully Oxidized TiO_2(110). *J. Phys. Chem. B* **2006**, *110*, 6229−6235.

(40) Stähler, J.; Rinke, P. Global and local aspects of the surface potential landscape for energy level alignment at organic-ZnO interfaces. *Chem. Phys.* **2017**, *485−486*, 149−165.

(41) Abraham, K. M. Electrolyte-Directed Reactions of the Oxygen Electrode in Lithium-Air Batteries. *J. Electrochem. Soc.* **2014**, *162*, A3021−A3031.

(42) Stähler, J.; Mehlhorn, M.; Bovensiepen, U.; Meyer, M.; Kusmierek, D. O.; Morgenstern, K.; Wolf, M. Impact of Ice Structure on Ultrafast Electron Dynamics in D_2O Clusters on Cu(111). *Phys. Rev. Lett.* **2007**, *98*, 206105.

(43) Gahl, C.*Elektronentransfer- und Solvatisierungsdynamik in Eis adsorbiert auf Metalloberflächen*. Ph.D. thesis, 2004.

(44) Fann, W. S.; Storz, R.; Tom, H. W. K.; Bokor, J. Electron thermalization in gold. *Phys. Rev. B* **1992**, *46*, 13592−13595.

(45) He, J.; Emtiaz, S.; Vidali, G. Measurements of Diffusion of Volatiles in Amorphous Solid Water: Application to Interstellar Medium Environments. *Astrophysical Journal* **2018**, *863*, 156.

(46) Mantina, M.; Chamberlin, A. C.; Valero, R.; Cramer, C. J.; Truhlar, D. G. Consistent van der Waals Radii for the Whole Main Group. *J. Phys. Chem. A* **2009**, *113*, 5806−5812.

(47) Skaf, M. S. Molecular dynamics simulations of dielectric properties of dimethyl sulfoxide: Comparison between available potentials. *J. Chem. Phys.* **1997**, *107*, 7996−8003.